communications chemistry

A Nature Portfolio journal

Article

https://doi.org/10.1038/s42004-026-02095-3

Multicomponent Betti reaction affords covalent organic framework nanoreactor for palladium-catalyzed nitroarene reduction

Neda Salarinejad[1], Mohammad Dinari[1] ✉, Jonas Lins[2], Torsten Gutmann[2,3] & Keun Hwa Chae[4]

Multicomponent reactions (MCRs) offer a sustainable and efficient pathway to complex molecular architectures. Here, we show the design and synthesis of a α-amino(2-hydroxybenzyl)-linked covalent organic framework (Betti-COF) *via* a one-pot, three-component solvothermal Betti reaction. This approach expands the scope of the MCR-based COF synthesis strategies by introducing a multicomponent pathway to highly ordered crystalline frameworks without the need for step-by-step linkage construction. The resulting *s*-Betti-COF exhibits a distinct hollow spherical morphology, high thermal stability, and robust porosity. This framework provides ideal support for the immobilization of small palladium nanoparticles (1-2 nm) within its pores to form the *s*-Betti-COF nanocomposite. The prepared samples were characterized by FT-IR, DNP-enhanced ^{13}C CP-MAS NMR, DNP-enhanced ^{15}N CP-MAS NMR, XRD, HR-TEM, FE-SEM, EDS, XPS, and nitrogen physisorption analysis. Kinetic investigations, including Hammett analysis, support a reaction mechanism involving an anionic intermediate. This study introduces the Betti reaction as a synthetic tool for constructing functional COFs and establishes these materials as highly effective nanoreactors for heterogeneous catalysis.

Multicomponent reactions (MCRs) are one-pot processes involving more than two reactants, typically three to seven readily available starting materials, in which most of the atoms from the starting materials are incorporated into the final products without the need for isolation or purification of intermediates[1,2]. MCRs inherently embody several green chemistry principles, offering unique synthetic advantages such as a high degree of atom economy, step and bond efficiency, simplified work-up procedures, environmentally benign reaction conditions, minimized potential contaminants, reduced reaction time, and often high product yields. The inherent advantage of MCRs lies in their ability to reduce synthetic steps through a one-pot approach. These reactions, performed in a single reaction vessel, often provide superior yields while generating fewer by-products. Another sustainable feature of MCRs is the in situ synthesis of reaction intermediates that rapidly convert to products, thus eliminating the need to isolate potentially unstable and toxic intermediates[3–5].

Covalent organic frameworks (COFs) have received considerable attention as versatile materials in various scientific fields. These frameworks consist of organic building blocks connected through strong covalent bonds between light elements from the periodic table, such as carbon, oxygen, nitrogen, and boron, which allow the construction of both two- and three-dimensional architectures[6–9]. COF materials have been successfully developed in various morphologies, including foams[10], sheets[11], spheres[12,13], fibers[14,15], cubes[16], shuttle[17], and belts[18]. COFs have remarkable properties, especially their excellent crystallinity, which can be precisely tailored by optimizing reaction conditions such as monomer addition rate, moderator usage, and the selection of acidic or basic catalysts. Furthermore, these materials feature low density, large surface areas, tunable pore size and structure, easily tailored functionality, and versatile covalent combinations of building blocks. These properties enable outstanding performance in applications including gas storage and separation[19,20], sensors[21], membrane technology[22], optoelectronics[23,24], catalysis[25,26], and functional device development[27].

Several synthetic approaches are employed in COF design and synthesis, including Aldol reactions[28], Knoevenagel condensation[29], heterocyclic ring formation (e.g., benzimidazole[30], benzothiazole[31], and benzoxazole[32]), Schiff base condensation[33], and imide[34] and aminal[35] bond

[1]Department of Chemistry, Isfahan University of Technology, Isfahan, 8415683111, Iran. [2]Eduard-Zintl Institute for Inorganic and Physical Chemistry, Technical University Darmstadt, Peter-Grünberg-Straße 8, Darmstadt, Germany. [3]Department of Chemistry, Paderborn University, Warburger Straße 100, Paderborn, Germany. [4]Advanced Analysis & Data Center, Korea Institute of Science and Technology (KIST), Seoul, Republic of Korea. ✉e-mail: dinari@iut.ac.ir

formations. Common preparation methods include solvothermal, mechanochemical[36,37], sonochemical[38], plasma induced[39], photochemical[40], microwave[41], electric-field mediated and electron beam irradiation methods[42,43]. The development of novel synthetic routes for the preparation of specific and increasingly complex COFs remains a central focus of materials science research.

Recent research has increasingly focused on using MCRs to synthesize COFs due to their green and sustainable properties. Several research groups have developed innovative MCR-based approaches. For example, ref. 44 successfully synthesized benzothiazole-linked COFs using an efficient one-pot, multicomponent, transition metal-free approach that demonstrated light-harvesting capacity as photosensitizers and enabled visible light-assisted carbon-boron bond cleavage. Wang et al.[45] used the Debus–Radziszewski reaction to construct ultra-stable imidazole-linked COFs. Thomas's group used both Povarov and Doebner multicomponent reactions to synthesize COFs with exceptional photocatalytic activity for hydrogen peroxide production and the selective photooxidation of benzylamine and aryl methyl sulfide derivatives[46]. Dong's group developed protocols using three-component, one-pot, in situ Strecker and Povarov reactions to synthesize α-aminonitrile- and quinoline-linked COFs[47]. Additionally, this research group introduced a simple and versatile strategy for constructing COFs using photocatalytic MCRs[48]. Under visible light irradiation, they successfully synthesized a series of robust COFs with excellent crystallinity and high porosity via the photoredox-catalyzed multicomponent Petasis reaction.

Based on these successful advancement in multicomponent COF construction, and our ongoing work in COF synthesis[49–52], we report the design and preparation of a COF via the Betti multicomponent reaction to form α-amino(2-hydroxybenzyl) linkages. This porous framework was subsequently used as a support for the immobilization of small palladium nanoparticles. The resulting nanocomposite material was investigated as an efficient catalyst for the reduction of nitroarenes. The structure, morphology, and chemical properties of the synthesized materials were extensively characterized using a combination of different analytical techniques.

Results and discussion

The synthesis of the target COF was based on Betti reaction a one-pot, three-component condensation of an aldehyde and an amine-functionalized building block and β-naphthol. To determine the optimal synthetic conditions, we investigated and compared two distinct synthetic approaches: a one-pot, three-component reaction and a sequential two-step reaction (Scheme 1). The one-pot, three-component reaction approach was conducted under both conventional heating in an oil bath (yielding *t*-Betti-COF) and solvothermal conditions (producing *s*-Betti-COF). To evaluate the efficiency of the three-component method, we also performed a two-step synthesis involving the initial formation and isolation of an imine intermediate, followed by its reaction with β-naphthol under solvothermal conditions.

Characterization of synthesized COFs

FT-IR spectroscopy was used to study the functional groups present in the synthesized structures (Fig. 1a). The spectrum of 2,4,6-tris(4-formylphenoxy)-1,3,5-triazine (TFPOT) showed strong absorption bands at 1701, 1569, and 1213 cm^{-1}, which correspond to the stretching vibrations of the formyl group (-CHO), the imine group (C=N) in the triazine structure, and the C-O bond, respectively. Additionally, weak bands at 2791 and 2834 cm^{-1} corresponding to the stretching vibrations of the C-H bond of the formyl group and other C-H bonds, respectively, were obtained. In the FT-IR spectrum of the *Im*-COF structure, the formyl group stretching absorption appeared as a weak band at 1730 cm^{-1}. This decrease in intensity indicates the significance of formyl groups in the TFPOT that were consumed during the formation of the imine. The appearance of a strong absorption band at 1638 cm^{-1} suggests imine formation and substantiates the successful reaction between *p*-phenylenediamine and TFPOT in the *Im*-COF structure. In the FT-IR spectra of the α-amino(2-hydroxybenzyl)-linked COFs (*t*-Betti-COF, *s*-Betti-COF, and *s*-Betti-COF_{2+1}), a peak at 3370 cm^{-1} appeared, which is attributed to O-H phenolic stretching vibrations. Furthermore, a medium peak at 3030 cm^{-1} became visible, which is associated with C-H aromatic stretching vibrations. Notably, the disappearance of the absorption band at 1638 cm^{-1} previously attributed to

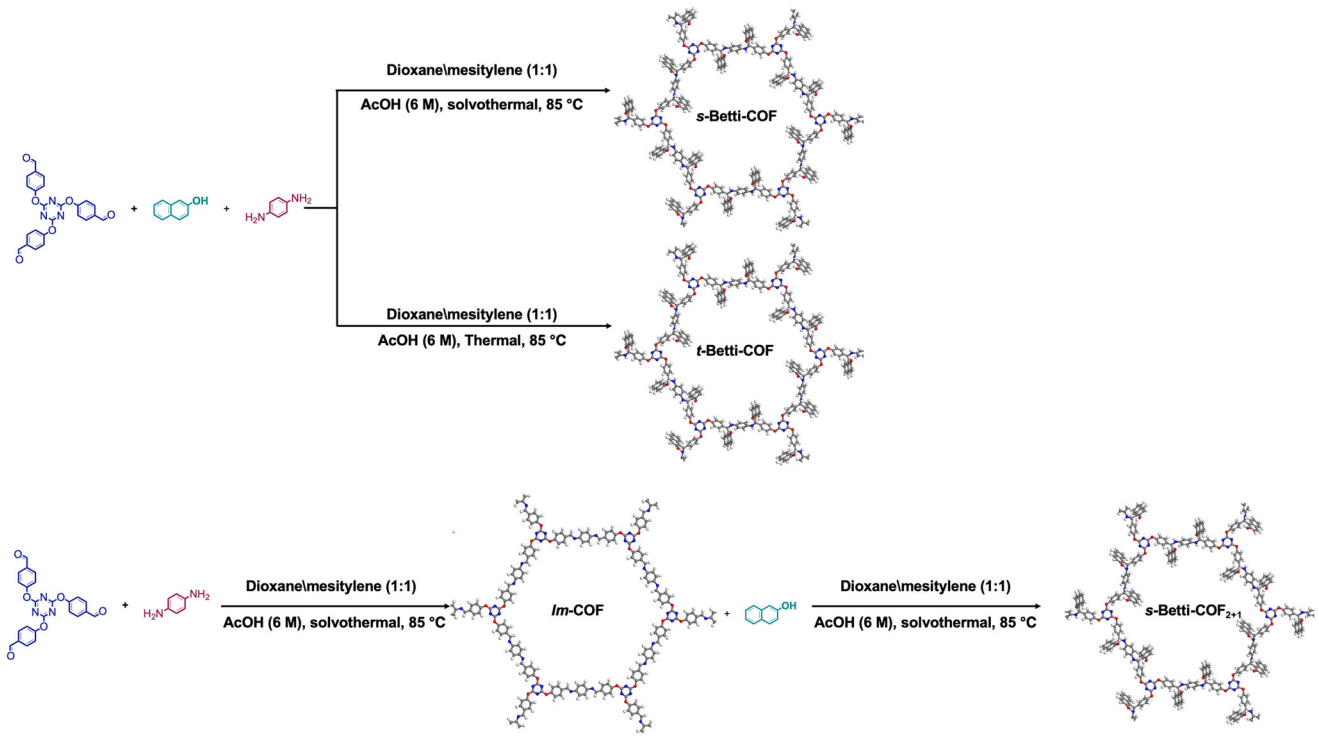

Scheme 1 | Schematic illustration of the synthesis of Betti-COFs. Synthesis of α-amino(2-hydroxybenzyl)-linked covalent organic frameworks (Betti-COFs).

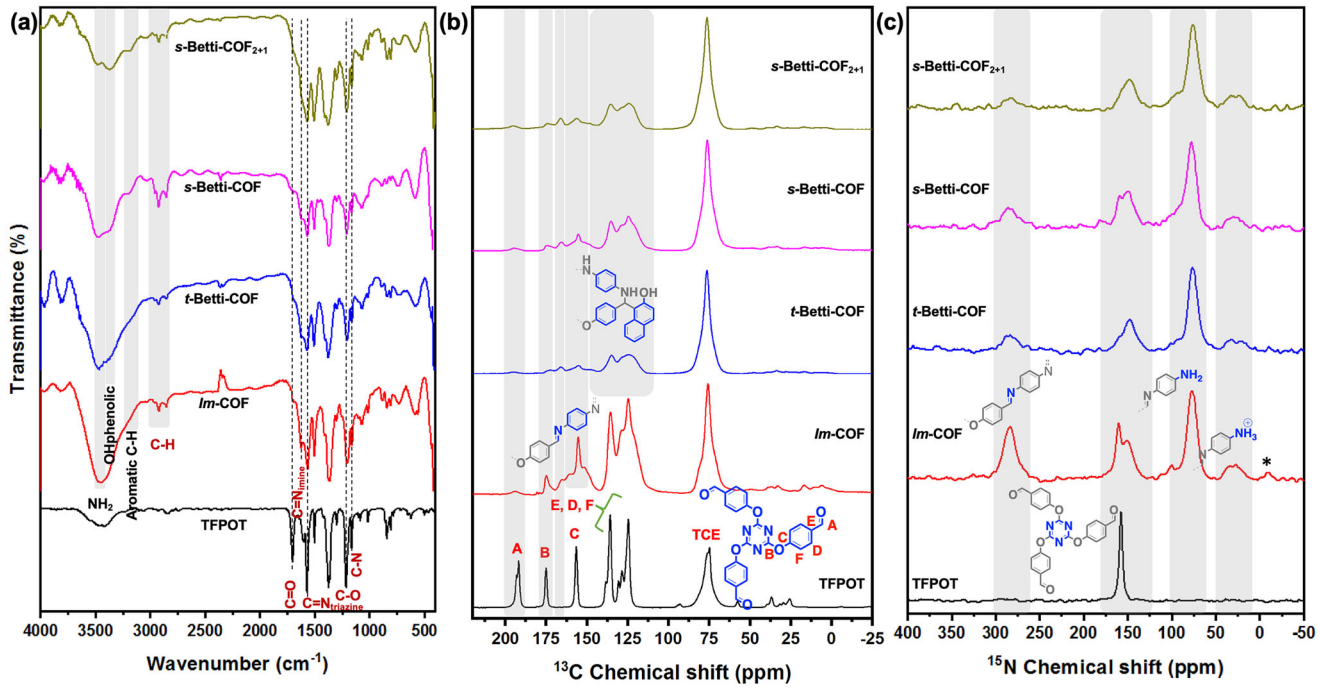

Fig. 1 | Spectroscopic characterization of the synthesized TFPOT and COFs. **a** FT-IR spectra, **b** DNP-enhanced ^{13}C CP-MAS NMR spectra, and **c** DNP-enhanced ^{15}N CP-MAS NMR spectra. Note: Spectra displayed in (**b**) were measured at 10 kHz spinning for TFPOT and at 12 kHz for *Im*-COF, *t*-Betti-COF, *s*-Betti-COF, and *s*-Betti-COF$_{2+1}$. Tiny signals in the range between −10 and 55 ppm obtained for the COF samples in (**b**) refer to spinning sidebands of the signal groups between 110 and 175 ppm. Tiny signals in the range between 20 and 100 ppm obtained for the TFPOT sample in (**b**) refer to spinning sidebands. The signal at 75 ppm in spectra **b** is assigned to TCE from the solvent matrix used for DNP sample preparation. Spectra displayed in **c** were measured at 10 kHz spinning for TFPOT, *t*-Betti-COF and *s*-Betti-COF$_{2+1}$, and at 12 kHz for *Im*-COF and *s*-Betti-COF. The signal marked with an asterisk (*) in **c** is attributed to a spinning sideband.

the imine provides evidence for the formation of the α-amino(2-hydroxybenzyl) structure.

Cross-polarization (CP) magic angle spinning (MAS) NMR, combined with dynamic nuclear polarization (DNP) were used to monitor the structure formation of the COFs (Fig. 1b, c) according to refs. 53,54. The DNP-enhanced ^{13}C CP-MAS NMR spectrum of the precursor TFPOT (Fig. 1b) displays the characteristic peaks at 192 and 175 ppm with their corresponding spinning sidebands, attributed to the formyl carbon (A) and triazine ring carbons (B), respectively[53–55]. The disappearance of the signal at 192 ppm and the appearance of a signal at 165 ppm in the DNP-enhanced ^{13}C CP-MAS NMR spectrum of *Im*-COF indicate that the formyl moiety has reacted successfully to form an imine group. Next, the DNP-enhanced ^{13}C CP-MAS NMR spectrum of *Im*-COF (Fig. 1b) shows an overlay of two signal patterns, one with a narrow line width, where signals at similar chemical shifts compared to TFPOT are visible and a broad one with dominating signals between 110 and 170 ppm. The narrow lines suggest the formation of ordered structures preserving moieties of TFPOT after the formation of *Im*-COF. The presence of broad signals next to the narrow ones clearly indicates the formation of disordered next to ordered structures. For the samples prepared with the Betti reaction, the broad component dominates the spectra, and no significant differences between *t*-Betty-COF, *s*-Betti-COF, and s-Betti-COF$_{2+1}$ are obtained. The broad peaks in the 110–140 ppm region are attributed to the overlapping contributions of both the aromatic carbons of the introduced naphthol moiety and the existing framework aromatic carbons. This let us assume that these materials contain similar structures, which is in good agreement with the IR data, where also no significant differences are obtained in the spectra.

The signals obtained in the DNP-enhanced ^{15}N CP-MAS NMR spectra (Fig. 1c) confirm the presence of nitrogen-containing functional groups in all samples. The DNP-enhanced ^{15}N CP-MAS NMR spectrum of the TFPOT precursor displays a single peak at 157 ppm, which corresponds to the nitrogen atoms in the triazine rings[56]. The DNP-enhanced ^{15}N CP-MAS NMR spectrum of *Im*-COF shows signals at 284, 159, 151, and 77 with a small peak at 98 ppm as a shoulder, and at 27 ppm. The signal at 284 ppm is attributed to imine groups showing a large anisotropy as underlined by the spinning sideband at −8 ppm marked with an asterisk. The signals at 159 (narrow peak) and 151 ppm (broad peak) most probably stem from triazine nitrogens in ordered and disordered structures, respectively, of the formed *Im*-COF[57] which is in agreement with the results obtained in the ^{13}C CP-MAS spectrum. In the Betti-COF series, the triazine nitrogen signals shift further upfield due to an altered electronic density distribution caused by two concurrent structural changes introduced by the Betti multicomponent reaction. First, the imine moieties transform into secondary amine moieties, which converts the sp^2-hybridized imine into an sp^3-hybridized secondary amine. This reduces conjugation through the framework and alters the electron density transmitted to the triazine ring. Second, the introduction of β-naphthol groups, which further modulate the electron density at the triazine ring through the extended conjugated framework. The signals at 77, and 27 ppm are assigned to unreacted amine groups from incompletely condensed precursor molecules present on the surface of the COF particles and to ammonium species from the protonation of the unreacted amine groups in an acidic reaction medium, respectively[58,59]. The DNP-enhanced ^{15}N CP-MAS NMR signals from imine and amine groups appeared similarly intense. However, this does not reflect their actual concentrations in the synthesized COF. This is because imine nitrogen atoms are more difficult to detect via ^{1}H → ^{15}N CP-MAS NMR since they do not have directly attached protons. The DNP enhancement technique preferentially amplifies signals from the surface of COF particles. Although the pores of the COF are large enough for the TEKPol molecules used for the sample preparation, diffusion of these molecules within the pores is likely slow. This slow diffusion results in a DNP enhancement gradient, which favors the detection of amine groups which are present on the surface of the COF particles. These amine groups are expected to be associated with incompletely condensed linkers[58]. The intensity of the signal at 284 ppm has decreased in the DNP-enhanced ^{15}N CP-MAS NMR spectra of Betti-COFs, which indicates the successful reaction between imine moieties and β-naphthol. Additionally, the peak for

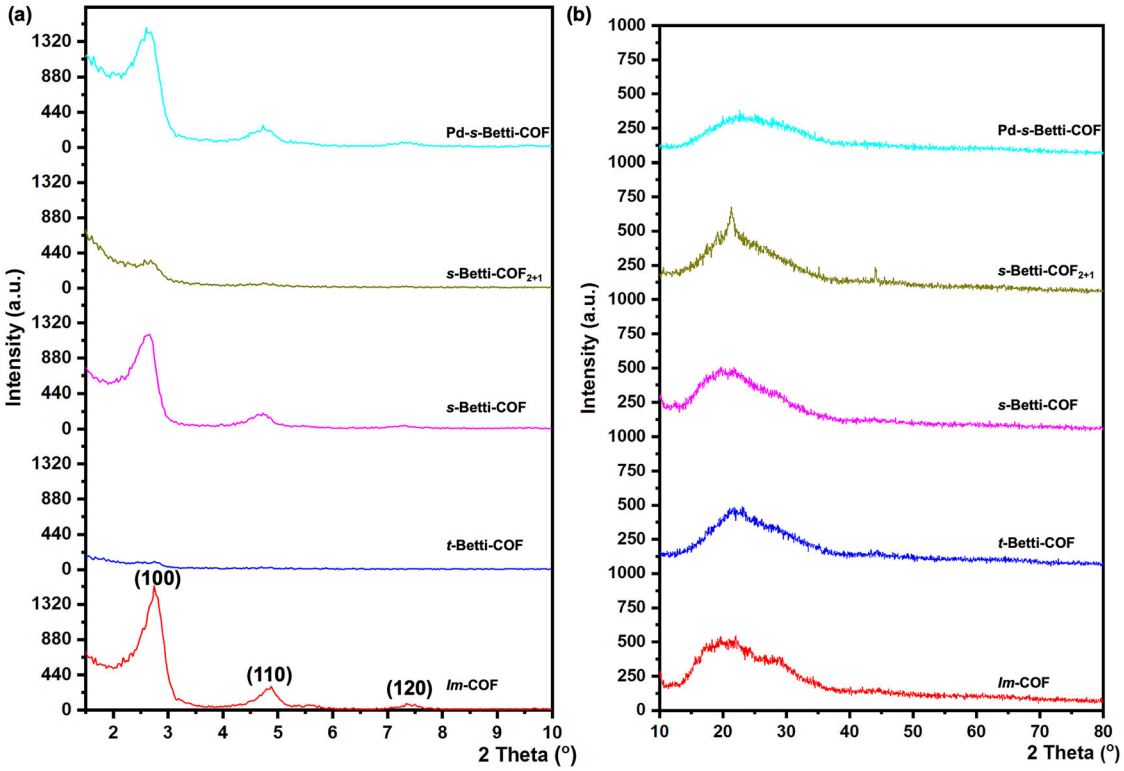

Fig. 2 | Crystallographic characterization of the synthesized COFs. a Low-angle and **b** wide-angle XRD patterns of synthesized COFs.

the secondary amine expected at around 55–60 ppm in the α-amino(2-hydroxybenzyl) linkage is not visible, which is probably because it overlaps with the peak from unreacted amine groups at 77 ppm[60,61].

X-ray diffraction (XRD) was used to investigate the phase purity and crystallinity of the synthesized structures (Fig. 2a, b). The crystallinity of the *Im*-COF was studied at a low angle (0.5–10°), which revealed well-defined diffraction features indicative of an ordered framework. The XRD pattern exhibited two distinct peaks at $2\theta = 2.70°$ and 4.84°, corresponding to the (100) and (110) crystal planes, respectively. An additional small peak at $2\theta = 7.43°$ was attributed to the (120) crystal plane. These results confirm the formation of a crystalline COF structure with long-range periodic ordering. The diffraction pattern of the *t*-Betti-COF showed a dramatic deterioration in crystallinity. The characteristic peaks observed in *Im*-COF disappeared completely, and the intensity of the peak at $2\theta = 2°$ decreased. This loss of crystalline order indicates an absence of a well-defined periodic framework, suggesting that the material should be classified as a covalent organic polymer (COP) rather than a crystalline COF. The poor crystallinity probably results from uncontrolled and rapid reaction kinetics inherent to thermal synthesis conditions. In contrast, the corresponding peaks were preserved in the XRD pattern of the *s*-Betti-COF structure, confirming that the COF synthesized under the three-component Betti reaction conditions, with the introduction of β-naphthol, maintained a crystalline framework. The diffraction pattern of the *s*-Betti-COF$_{2+1}$ exhibited reduced peak intensities, suggesting lower crystallinity and this material is similarly classified as a COP. This reduced crystallinity can be attributed to the disruption of the crystalline framework caused by the incorporation of β-naphthol into the *Im*-COF structure. The superior crystallinity observed in the three-component, one-pot synthesis of *s*-Betti-COF structure can be explained by slower crystallization kinetics in the solvothermal environment, allowing development of a more ordered structure with enhanced specific surface area and improved porosity, ultimately yielding a true COF[62,63]. This comparison demonstrates that the synthesis pathway critically determines the structural outcome of Betti-COF materials. Comparative analysis of the low-angle diffraction patterns of the *s*-Betti-COF and *Im*-COF structures revealed a slight shift in the diffraction angle of the (100) plane from 2.70° to 2.63° (Fig. S1). This minor shift can be attributed to the structural changes in interplanar spacing and unit cell parameters, as well as to rigidification, which occurred following the formation of the α-amino(2-hydroxybenzyl) linkages[64]. To elucidate the crystalline structure of the synthesized *s*-Betti-COF, 2D-layered structures with staggered AB and eclipsed AA stacking arrangements were modeled using Materials Studio software V. 24.1 (Fig. S2). The experimental XRD pattern showed better agreement with the simulated pattern obtained from the AA eclipsed structure compared to the AB staggered structure. The optimal lattice parameters obtained through refinement for the unit cell in the space group of *P*1 are as follows: a = 7.42 Å, b = 39.29 Å, c = 37.95 Å, α = 120°, and β = γ = 90°. For comparison, the interlayer spacing of the parent *Im*-COF is 3.44 Å, consistent with the typical π-π stacking distances reported for imine-linked 2D COFs (Table S3). The interlayer spacing in *s*-Betti-COF is nearly double that of the parent *Im*-COF (7.42 vs 3.44 Å), which is attributable to the introduction of the bulky β-naphthol moieties via the Betti reaction. These large aromatic substituents lead to an increased interlayer space between adjacent 2D COF sheets. This phenomenon is well documented in the literature for COFs functionalized with sterically demanding substituents, where interlayer spacing substantially exceeding the typical π-π stacking distances of ~3.5 Å has been reported[65,66]. Furthermore, the broad peak observed at approximately $2\theta = 20°$ in the wide-angle XRD pattern (10–80°) indicates the formation of isoreticular 2D-layered structures stacking in the *c*-direction (Fig. 2b)[46]. Consequently, *s*-Betti-COF -the only Betti-COF retaining true COF crystallinity- was selected as the support for palladium immobilization due to its crystalline architecture. After immobilization of palladium nanoparticles on *s*-Betti-COF, the XRD patterns in both low- and wide-angle remained unchanged. This preservation of the diffraction patterns can be attributed to the low loading of palladium, which was insufficient to cause a detectable change in the crystalline structure of COF. The absence of the characteristic diffraction peaks of palladium nanoparticles in the XRD pattern could be attributed to the low metal loading, the high dispersion, and the small size of the nanoparticles.

Nitrogen physisorption analysis was conducted to evaluate the surface area, pore characteristics, and average pore diameter of the synthesized

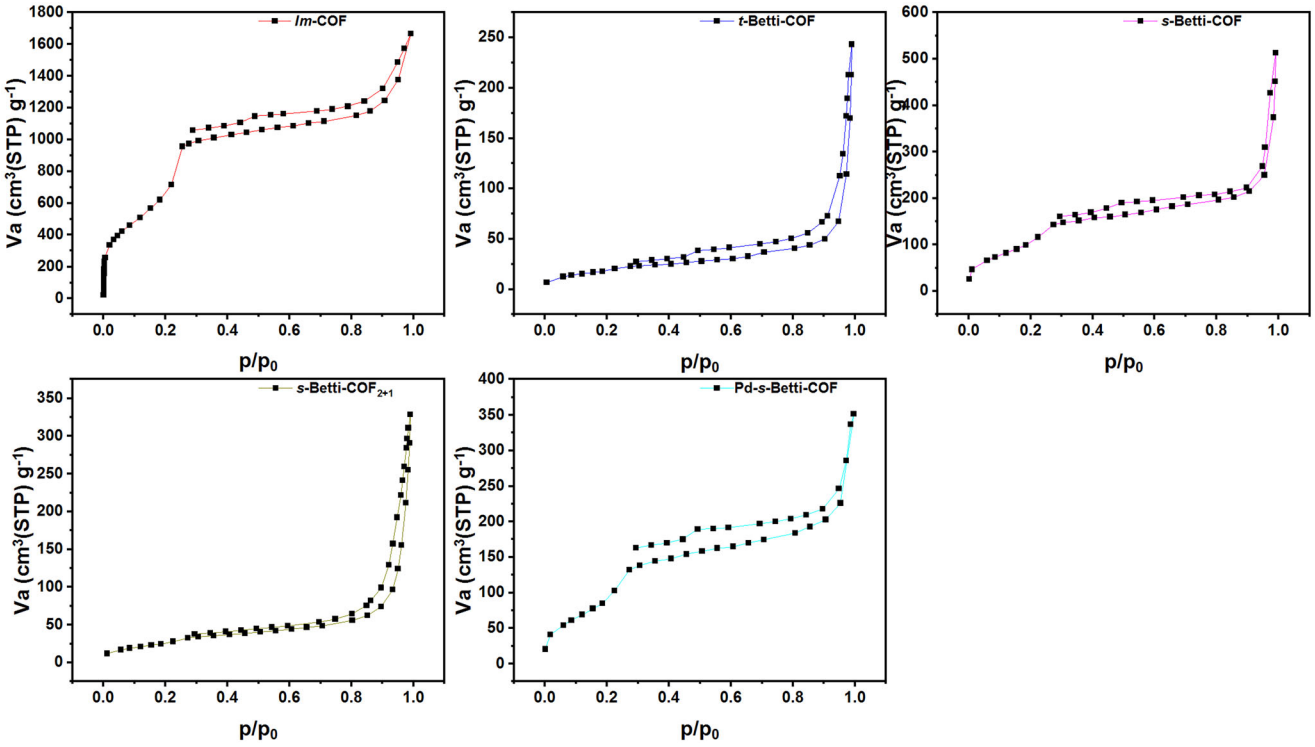

Fig. 3 | Textural properties of the synthesized COFs. Nitrogen adsorption-desorption isotherms of the synthesized COFs were measured at 77 K.

structures (Fig. 3). The N_2 adsorption and desorption isotherms of all synthesized COFs exhibited type IV behavior with a hysteresis loop, confirming the presence of mesopores and the associated capillary phenomena. The *Im*-COF exhibits a combination Type I and Type IV isotherms with a sharp uptake of nitrogen at low relative pressure ($p/p_0 < 0.05$), indicating microporosity[67]. An open hysteresis loop was also observed, suggesting a broad pore size distribution or a complex network of interconnected pores that prevented uniform adsorption and desorption processes across all pores. This resulted in delayed desorption and the characteristic open loop[68–70]. The specific surface area measured by the BET method was 2911 m^2g^{-1} (Table S1). For the Betti-COFs, the characteristic steep nitrogen uptake at low pressures ($p/p_0 < 0.05$) disappeared, indicating an absence of micropores in these derivatives. Additionally, the hysteresis loops closed completely, demonstrating improved uniformity and a narrower pore size distribution. All three samples exhibited a substantial decrease in surface area following the Betti reaction. This reduction in surface area and decrease in pore volume provide strong evidence that the imine bonds successfully reacted through the reaction with β-naphthol, resulting in the naphthol moieties occupying the pore volume (Table S1). However, the solvothermal method (*s*-Betti-COF) produced a COF with a larger surface area than the thermal method (*t*-Betti-COF), suggesting that superior structural ordering was achieved under solvothermal conditions. When comparing the one-pot three-component solvothermal method (*s*-Betti-COF, 500.6 m^2/g) with the two-step sequential method (s-Betti-COF_{2+1}, 110.7 m^2/g), the results showed significant differences. The stepwise approach likely disrupts optimal framework formation due to the partial collapse of the initial imine framework and the less-ordered integration of the β-naphthol component when it is added sequentially. This results in the formation of larger, less uniform pores at the expense of smaller, more numerous pores. Following palladium immobilization on *s*-Betti-COF, the surface area did not change, while the pore volume decreased by ~30%, and this introduced an open hysteresis loop in the nitrogen isotherm. These observations strongly suggest that the palladium was successfully incorporated into the pores of the COF and occupied them rather than being deposited on the surface. The open hysteresis loop indicates that the palladium may have partially blocked the pores or altered their connectivity, resulting in delayed nitrogen release during desorption. The high mean pore diameter in *s*-Betti-COF_{2+1} and *t*-Betti-COF indicated that these COFs had different crystallinity, morphology and porosity compared to *Im*-COF and *s*-Betti-COF, which was confirmed by XRD and microscopic analysis (Fig. 2a and Fig. S7).

X-ray photoelectron spectroscopy was used to evaluate the surface composition and determine the electronic states of the elements (Fig. S5). The survey spectra of *s*-Betti-COF revealed the presence of C 1s, N 1s, and O 1s core levels (Fig. S5a). Additionally, Pd-*s*-Betti-COF showed Pd 3d signals, confirming successful palladium incorporation. High-resolution analysis of the N 1s region of *s*-Betti-COF revealed four distinct components at binding energies of 398.62, 398.81, 399.70, and 400.55 eV (Fig. S5b). These were assigned to triazine C=N, imine C=N, Betti linkage C-NH-C, and dangling NH_2, respectively[49,71]. The Pd $3d_{5/2}$ core level was deconvoluted into two components at 335.83 eV (73.2%) and 337.72 eV (26.8%), which corresponded to Pd^0 and Pd^{2+} (as PdO) species, respectively (Fig. S5c). These results indicate that a large proportion of the palladium is reduced by the reductive annealing process. The presence of palladium oxide also indicates the surface oxidation of the palladium nanoparticles in the presence of air.

The thermal gravimetric analysis of *Im*-COF, *s*-Betti-COF and Pd-*s*-Betti-COF was performed. The TGA profiles showed no obvious weight losses of *Im*-COF, *s*-Betti-COF, and Pd-*s*-Betti-COF up to ~400 °C, indicating their good thermal stability (Fig. S6). The slight increase in weight during the initial stage of thermolysis is due to the buoyancy effect of the TGA equipment, which affects the apparent mass during TGA analysis[72,73]. The enhanced thermal stability of Pd-*s*-Betti-COF could be related to the hydrogen reduction annealing process, which drives the elimination of residual solvent molecules and labile surface species at 200 °C.

The morphology characteristics of the synthesized structures were evaluated by field emission-scanning electron microscopy (FE-SEM) (Fig. 4 and Fig. S7). The FE-SEM image of the *Im*-COF revealed a uniform spherical morphology with a diameter of about 1.4 μm. In contrast, the FE-SEM image of the *t*-Betti-COF exhibited a distinct morphological change from spherical to tubular structures. This transformation is probably attributed to the change in the reaction environment under thermal conditions. In the solvothermal method, homogeneous nucleation typically results in zero-dimensional spherical growth, leading to the resulting spherical structures

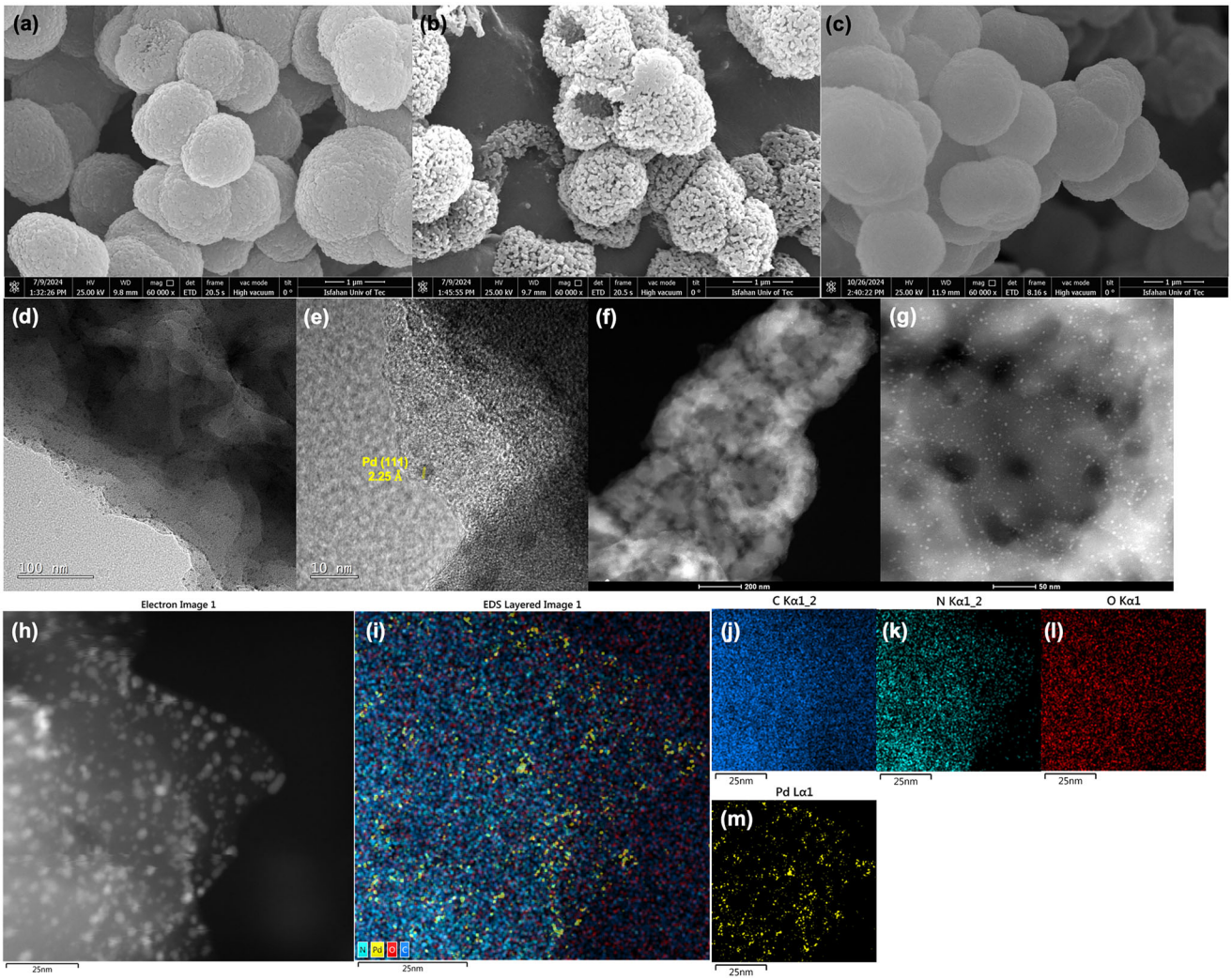

Fig. 4 | Morphological and elemental characterization of the synthesized COFs. FE-SEM images of **a** *Im*-COF, **b** *s*-Betti-COF, **c** Pd-*s*-Betti-COF, **d** bright-field TEM, **e** HR-TEM, **f**–**h** dark-field of Pd-*s*-Betti-COF, and **i**–**m** corresponding quantitative EDS mapping.

(Fig. S7a). This significant structural change was corroborated by N_2 physisorption analysis, which confirmed accompanying changes in shape and porosity. The FE-SEM image of the s-Betti-COF_{2+1} shows that the original morphology was preserved relative to the *Im*-COF (Fig. S7b). This suggests that the sequential addition of β-naphthol did not disrupt the fundamental structural architecture. The morphology did not change after palladium was immobilized on *s*-Betti-COF (Fig. 4c). Transmission electron microscopy (TEM) images of *s*-Betti-COF revealed hollow spherical structures (Fig. S8). Bright-field and dark-field TEM images of Pd-*s*-Betti-COF show that small palladium nanoparticles (~1–2 nm) were immobilized inside the *s*-Betti-COF pores. The high-resolution TEM (HR-TEM) image displayed a lattice spacing of 2.25 Å for the Pd metallic nanoparticles, indicating the crystalline nature of the palladium nanoparticles with (111) d-spacing (Fig. 4e). Energy-dispersive X-ray spectroscopy analysis of the Pd-*s*-Betti-COF reveals that the palladium nanoparticles are closely associated with nitrogen and carbon atoms, indicating that the organic moieties surround the palladium nanoparticles (Fig. 4i–m).

Catalytic performance of Pd-s-Betti-COF

Reduction of p-nitroaniline. The catalytic activity of the synthesized Pd-*s*-Betti-COF catalyst was evaluated on sodium borohydride-mediated reduction of nitroarenes. To determine the optimal conditions, initial experiments were conducted with varying amounts of sodium borohydride with 1 mg of Pd-*s*-Betti-COF. Initially, the reaction rates increased proportionally with sodium borohydride concentration; after reaching a maximum, the rate constant decreased (Fig. S9). The initial increase in reaction rate with sodium borohydride concentration is attributed to the greater availability of reducing agent to react with *p*-nitroaniline. The subsequent decrease at higher sodium borohydride can be attributed to a change in pH of the solution at high sodium borohydride concentrations, resulting in a decreased rate of hydrolysis[74].

Substituent effects on the reduction of nitroarenes reactivity and the Hammett plot. The effect of substituent groups on the reactivity of nitroarenes in the reduction reaction was investigated using various nitroarene derivatives (Figs. S10 and S11). The first study investigated nitroarene derivatives with electron-releasing groups such as *o*-nitroaniline, *m*-nitroaniline, *p*-nitroaniline, *N,N*-dimethyl-4-nitroaniline, *p*-nitroanisole, and *p*-nitrotoluene. These derivatives demonstrated good reactivity in the reduction process. The reactivity patterns of nitroaniline derivatives clearly demonstrate the influence of electronic resonance effects (Fig. 5a). The *meta*-substituted isomer showed higher reactivity than the *ortho*- and *para*-isomers. This suggests that the reaction mechanism involves negatively charged species, since an amino group in the meta position cannot destabilize these species through resonance effects.

Additionally, nitroarenes containing electron-withdrawing substituents, including halogens (fluoro and bromo) and carboxyl groups positioned on the aromatic ring, were examined under the same catalytic

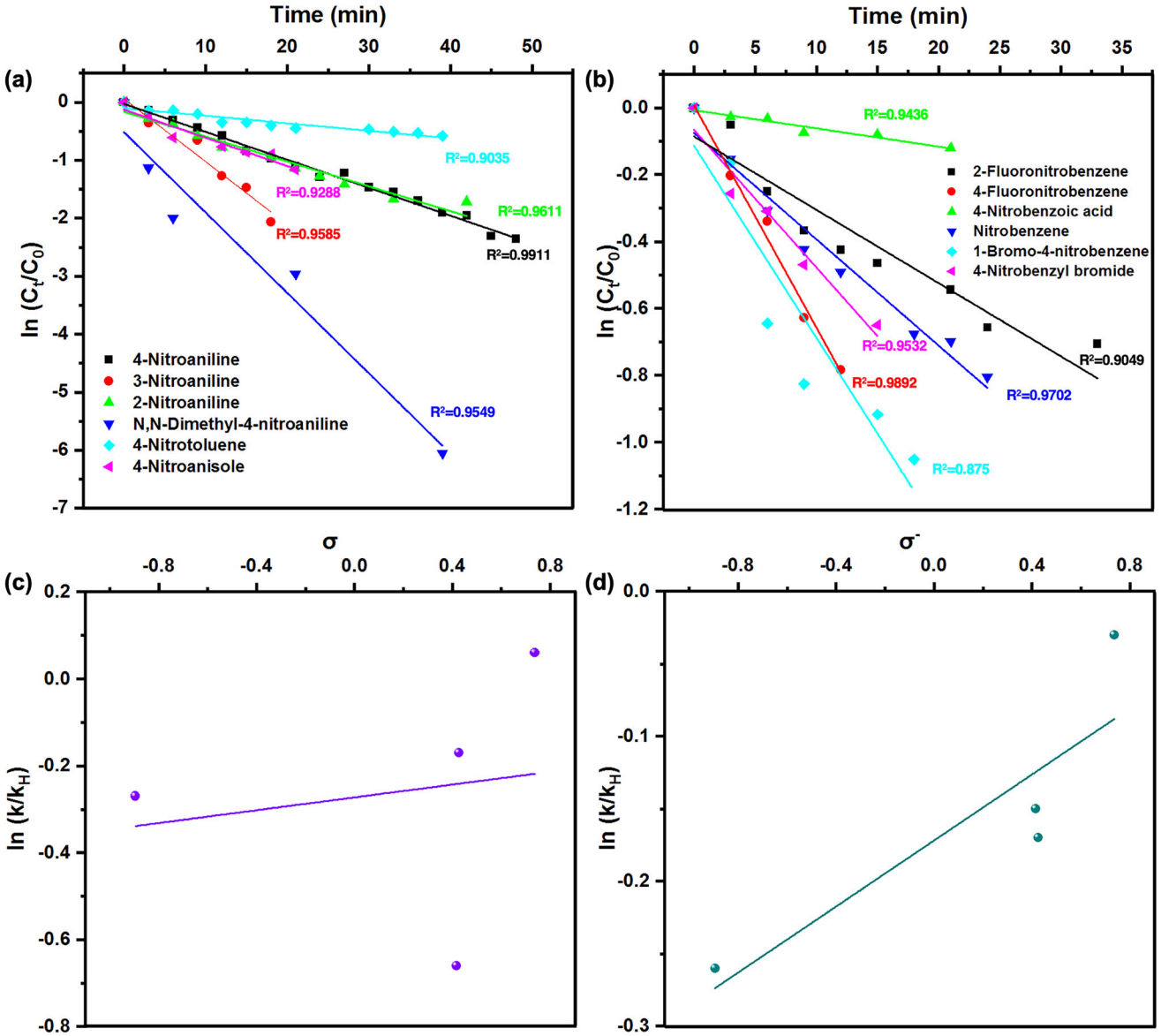

Fig. 5 | Substituent effects and Hammet analysis for the catalytic reduction of nitroarenes. The influence of **a** electron-releasing, **b** electron-withdrawing groups, on the reduction of nitroarenes, **c**, **d** Hammett plots for the reduction of *p*-substituted nitroarenes.

reaction conditions (Fig. 5b). UV-Vis spectroscopic analysis of the halogenated derivatives showed no characteristic aniline absorption peak at 230 nm, confirming that dehalogenation did not occur during the reduction process (Fig. S11).

The reactivity of catalytic substrates is fundamentally determined by the distribution of charge density at their reaction centers. To elucidate the mechanistic pathway of the reduction of nitroarenes, the reaction rates were calculated for a series of *para*-substituted nitroarene derivatives. Using the Hammett equation, a linear free energy relationship was established for the competitive reduction of *para*-substituted nitroarenes with sodium borohydride. The correlation parameters were calculated to be $\rho \approx 0.0738$, $R^2 = 0.0318$ (using σ values) and $\rho \approx 0.1139$, $R^2 = 0.7625$ (using σ^- values) (Fig. 5c, d). Positive ρ values indicate that the catalytic reduction proceeds through anionic intermediates and that electron-withdrawing groups enhance the rate of nitroarene reduction. The superior correlation coefficient obtained using σ^- values reflects direct resonance interactions between the substituents and the anionic reaction center. This observation is consistent with previous reports on positive ρ values[75,76] and their correlation with σ^- values.

Thermodynamic study of the kinetics of the reduction of p-nitroaniline. Temperature gradient studies were conducted across a range of 10 to 50 °C (Fig. 6a). Following Arrhenius theory, ln k was plotted against 1/T (Fig. 6b). The Arrhenius activation energy (E_a) was determined using the Arrhenius equation, and the thermodynamic parameters, including the enthalpy of activation ($\Delta H^{\ddagger}$) and the entropy of activation ($\Delta S^{\ddagger}$), were calculated using Eyring equation. The constants used were: A (pre-exponential factor), R (universal gas constant, 8.314 J.mol^{-1}.K^{-1}), k_B (Boltzmann constant, 1.38×10^{-23} J.K^{-1}) and h (Planck constant, 6.626×10^{-34} J.s).

$$\ln k = \ln A - \frac{E_a}{RT} \quad \text{Arrhenius Equation}$$

$$\ln \frac{k}{T} = \ln \frac{k_B}{h} + \frac{\Delta S^{\ddagger}}{R} - \frac{\Delta H^{\ddagger}}{R}\left(\frac{1}{T}\right) \quad \text{Eyring Equation}$$

The reaction rate constants showed a positive correlation with temperature. Analysis of the Arrhenius plot (ln k vs 1/T) revealed an activation

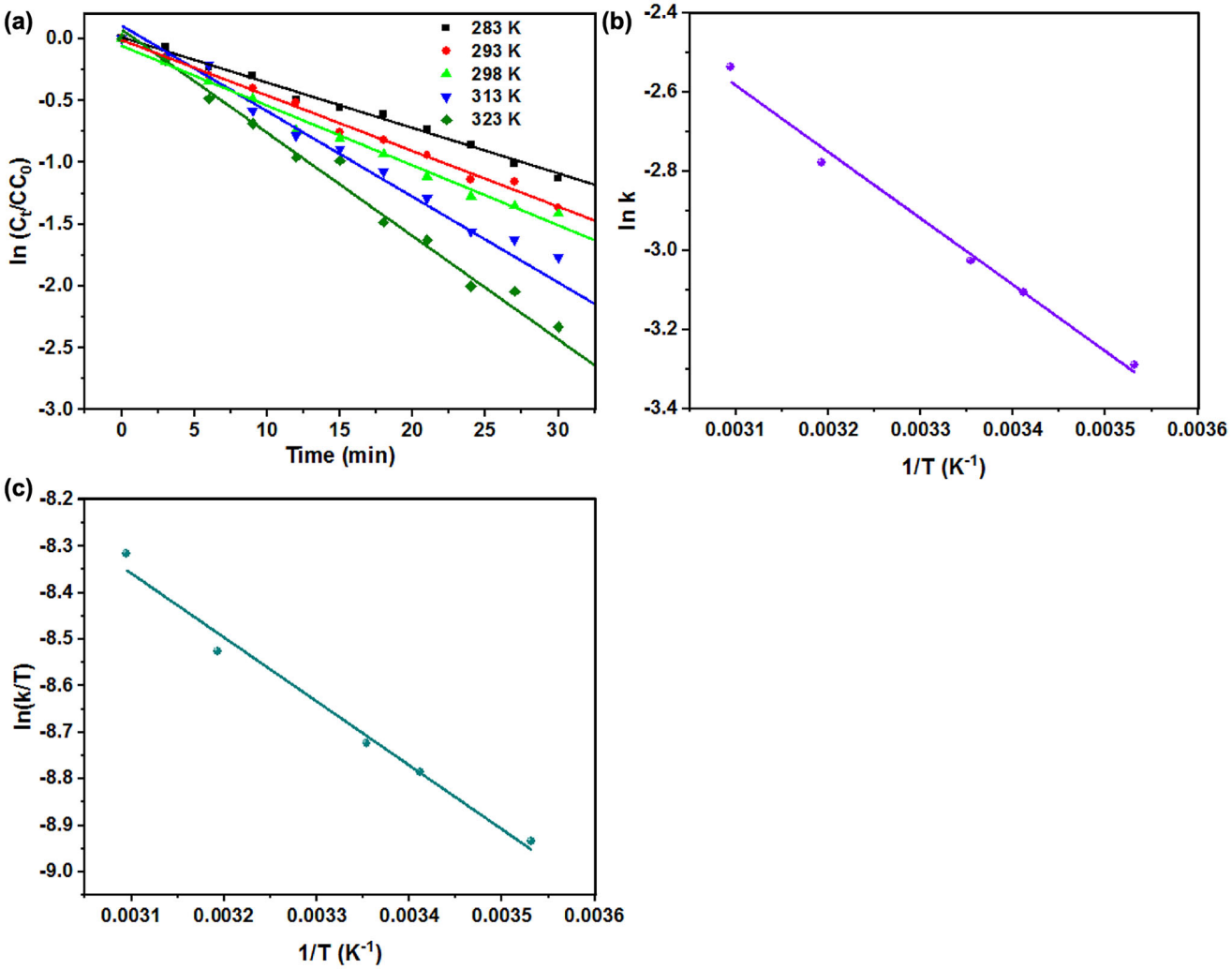

Fig. 6 | Thermodynamic and kinetic study of *p*-nitroaniline reduction. a The effect of temperature on reduction of *p*-nitroaniline over Pd-s-Betti-COF, **b** Arrhenius plot of ln k vs. 1/T, and **c** Eyring–Polanyi plot of ln(k/T) vs 1/T.

energy (E_a) of 13.95 kJ.mol^{-1} for the reduction of p-nitroaniline. Thermodynamic parameters were extracted from the slope and intercept of the ln(k/T) vs 1/T plot (Fig. 6c). The ($\Delta H^{\ddagger}$) and ($\Delta S^{\ddagger}$) values were calculated to be 11.43 kJ.mol^{-1} and −250.73 J.mol^{-1}K^{-1}, respectively. The positive value of $\Delta H^{\ddagger}$ confirms the endothermic nature of the reduction reaction, consistent with the observed temperature-dependent increase in rate constants. The negative $\Delta S^{\ddagger}$ value suggests increased structural ordering at the catalyst-solution interface during the transition state.

Catalyst reusability and durability are crucial factors for commercial implementation. To evaluate these properties, the Pd-based catalyst was examined through consecutive cycles of the reduction of p-nitroaniline. The catalyst maintained its performance across seven consecutive cycles without a significant decline in catalytic activity (Fig. S12a). ICP-OES analysis was employed on the reaction solution to assess metal leaching and revealed minimal palladium leaching of only 0.5% after four cycles. Post-reaction characterization using FT-IR, N_2 physiosorption, and XRD analysis confirmed that the catalyst's structure remained largely intact after four successive runs (Fig. S12). The increased surface area after reuse was probably due to the ultrasonication during washing of the catalyst after each run. The appearance of the characteristic peak of the imine bond at1600 cm^{-1} in the post-cycling FT-IR spectrum probably indicated the formation of imine linkages between the residual unreacted aldehyde groups present on the COF surface and the aniline derivatives generated during the nitroarene reduction reaction.

Conclusion

In summary, this research successfully demonstrates the application of the Betti multicomponent reaction as an efficient strategy for the synthesis of an α-amino(2-hydroxylbenzyl)-linked COF. The optimal method was identified as the one-pot, three-component solvothermal process (*s*-Betti-COF), yielding a thermally stable *s*-Betti-COF with a unique hollow spherical morphology and accessible porosity. This COF is an excellent platform for the immobilization of palladium nanoparticles and synthesizing a robust Pd-*s*-Betti-COF nanocomposite. The catalyst exhibited excellent activity, selectivity, and recyclability in the reduction of nitroarenes, with minimal metal leaching over successive cycles. Kinetic and mechanistic studies provided valuable insights into the reaction pathway and confirmed the role of electron-withdrawing groups in accelerating the reaction via anionic intermediates. Additionally, the prepared samples were characterized by FT-IR, DNP-enhanced ^{13}C CP-MAS NMR, DNP-enhanced ^{15}N CP-MAS NMR, XRD, HR-TEM, FE-SEM, EDS, XPS, and nitrogen physisorption analysis. This work expands the scope of multicomponent reactions in the rational design of functional materials and highlights the significant potential of the resulting COFs as heterogeneous catalyst supports. This opens avenues for developing sustainable chemical processes.

Data availability

The data that support the findings of this study are available within the article or the Supplementary Information file. Additional data related to this

paper may be available from the corresponding authors upon reasonable request.

The source data for Fig. 1 is in Supplementary Data Fig. 1
The source data for Fig. 2 is in Supplementary Data Fig. 2
The source data for Fig. 3 is in Supplementary Data Fig. 3
The source data for Fig. 4 is in Supplementary Data Fig. 4
The source data for Fig. 5 is in Supplementary Data Fig. 5
The source data for Fig. 6 is in Supplementary Data Fig. 6

Received: 24 December 2025; Accepted: 4 June 2026;
Published online: 21 June 2026

References

1. Dömling, A., Wang, W. & Wang, K. Chemistry and biology of multicomponent reactions. *Chem. Rev.* **112**, 3083–3135 (2012).
2. Dömling, A. Recent developments in isocyanide based multicomponent reactions in applied chemistry. *Chem. Rev.* **106**, 17–89 (2006).
3. Slobbe, P., Ruijter, E. & Orru, R. V. A. Recent applications of multicomponent reactions in medicinal chemistry. *Med. Chem. Commun.* **3**, 1189–1218 (2012).
4. Cioc, R. C., Ruijter, E. & Orru, R. V. A. Multicomponent reactions: advanced tools for sustainable organic synthesis. *Green Chem.* **16**, 2958–2975 (2014).
5. Biggs-Houck, J. E., Younai, A. & Shaw, J. T. Recent advances in multicomponent reactions for diversity-oriented synthesis. *Curr. Opin. Chem. Biol.* **14**, 371–382 (2010).
6. Yazdani, H., Hooshmand, S. E. & Varma, R. S. Covalent organic frameworks and multicomponent reactions: an endearing give-and-take relationship. *Org. Chem. Front.* **9**, 4178–4191 (2022).
7. El-Kaderi, H. M. et al. Designed synthesis of 3d covalent organic frameworks. *Science* **316**, 268–272 (2007).
8. Ding, S.-Y. & Wang, W. Covalent organic frameworks (COFs): from design to applications. *Chem. Soc. Rev.* **42**, 548–568 (2012).
9. Raghav, S. et al. Recent advancements in synthesis and applications of covalent organic frameworks. *Appl. Mater. Today* **44**, 102694 (2025).
10. Mohammed, A. K. et al. Connecting microscopic structures, mesoscale assemblies, and macroscopic architectures in 3D-printed hierarchical porous covalent organic framework foams. *J. Am. Chem. Soc.* **142**, 8252–8261 (2020).
11. Rodríguez-San-Miguel, D., Montoro, C. & Zamora, F. Covalent organic framework nanosheets: preparation, properties and applications. *Chem. Soc. Rev.* **49**, 2291–2302 (2020).
12. Ma, W. et al. Size-controllable synthesis of uniform spherical covalent organic frameworks at room temperature for highly efficient and selective enrichment of hydrophobic peptides. *J. Am. Chem. Soc.* **141**, 18271–18277 (2019).
13. Liu, Y.-Y. et al. Self-templated synthesis of uniform hollow spheres based on highly conjugated three-dimensional covalent organic frameworks. *Nat. Commun.* **11**, 5561 (2020).
14. Huang, W. et al. Solvothermal synthesis of microporous, crystalline covalent organic framework nanofibers and their colorimetric nanohybrid structures. *ACS Appl. Mater. Interfaces* **5**, 8845–8849 (2013).
15. Wang, S. et al. Reversible polycondensation-termination growth of covalent-organic-framework spheres, fibers, and films. *Matter* **1**, 1592–1605 (2019).
16. Wan, S., Guo, J., Kim, J., Ihee, H. & Jiang, D. A photoconductive covalent organic framework: self-condensed arene cubes composed of eclipsed 2D polypyrene sheets for photocurrent generation. *Angew. Chem. Int. Ed.* **48**, 5439–5442 (2009).
17. Lu, Z. et al. A hollow microshuttle-shaped capsule covalent organic framework for protein adsorption. *J. Mater. Chem. B*. **7**, 1469–1474 (2019).
18. Wan, S., Guo, J., Kim, J., Ihee, H. & Jiang, D. A belt-shaped, blue luminescent, and semiconducting covalent organic framework. *Angew. Chem. Int. Ed*. **47**, 8826–8830 (2008).
19. Li, B., Wen, H.-M., Zhou, W. & Chen, B. Porous metal–organic frameworks for gas storage and separation: what, how, and why? *J. Phys. Chem. Lett.* **5**, 3468–3479 (2014).
20. Zhu, L. & Zhang, Y.-B. Crystallization of covalent organic frameworks for gas storage applications. *Molecules* **22**, 1149 (2017).
21. Yue, Y., Ji, D., Liu, Y. & Wei, D. Chemical Sensors based on covalent organic frameworks. *Chem. Eur. J.* **30**, e202302474 (2024).
22. Yuan, S. et al. Covalent organic frameworks for membrane separation. *Chem. Soc. Rev.* **48**, 2665–2681 (2019).
23. Keller, N. & Bein, T. Optoelectronic processes in covalent organic frameworks. *Chem. Soc. Rev.* **50**, 1813–1845 (2021).
24. Huang, W., Zhang, W., Yang, S., Wang, L. & Yu, G. 3D covalent organic frameworks from design, synthesis to applications in optoelectronics. *Small* **20**, 2308019 (2024).
25. Guo, J. & Jiang, D. Covalent organic frameworks for heterogeneous catalysis: principle, current status, and challenges. *ACS Cent. Sci.* **6**, 869–879 (2020).
26. Yusran, Y., Li, H., Guan, X., Fang, Q. & Qiu, S. Covalent organic frameworks for catalysis. *EnergyChem* **2**, 100035 (2020).
27. Chen, G. et al. Recent advances in functional electronic devices enabled by two-dimensional covalent organic framework films. *Mater. Chem. Front.* **9**, 1443–1458 (2025).
28. Xu, X., Feng, Y., Chen, H. & Huang, N. Semiconducting polyaromatic covalent organic frameworks constructed through self-aldol condensation. *J. Am. Chem. Soc.* **147**, 16653–16660 (2025).
29. Meng, F., Bi, S., Sun, Z., Wu, D. & Zhang, F. 2, 4, 6-Trimethylpyridine-derived vinylene-linked covalent organic frameworks for confined catalytic esterification. *Angew. Chem. Int. Ed.* **61**, e202210447 (2022).
30. Asadi, P., Falsafin, M. & Dinari, M. Construction of new covalent organic frameworks with benzimidazole moiety as Fe3+ selective fluorescence chemosensors. *J. Mol. Struct.* **1227**, 129546 (2021).
31. Kim, Y. H. et al. Benzothiazole-based covalent organic frameworks with different symmetrical combinations for photocatalytic CO2 conversion. *Chem. Mater.* **33**, 8705–8711 (2021).
32. Liang, E. et al. Structure fine-tuning of benzoxazole-linked covalent organic frameworks (COFs) for photocatalytic hydroxylation of phenyl boronic acids. *J. Mater. Chem. A* **13**, 16749–16758 (2025).
33. Li, W., Li, J., Wen, G., Li, C. & Jiang, Z. Simple Schiff-base covalent organic framework nanoprobe for resonance Rayleigh scattering detection of trichlorophenol. *Langmuir* **41**, 11711–11721 (2025).
34. Zhao, W. et al. Water-assisted microwave synthesis of imide-linked covalent organic frameworks in minutes. *J. Am. Chem. Soc.* **147**, 16319–16330 (2025).
35. Guo, R. et al. Aminal-linked covalent organic framework membranes achieve superior ion selectivity. *Small* **20**, 2308904 (2024).
36. Krusenbaum, A., Grätz, S., Tamiru Tigineh, G., Borchardt, L. & Gon Kim, J. The mechanochemical synthesis of polymers. *Chem. Soc. Rev.* **51**, 2873–2905 (2022).
37. Pickhardt, W., Grätz, S. & Borchardt, L. Direct mechanocatalysis: using milling balls as catalysts. *Chem. Eur. J.* **26**, 12903–12911 (2020).
38. Koo, S. & Kang, D. W. Emerging porous solids and sonochemistry. *CrystEngComm* **25**, 5994–6005 (2023).
39. He, J. et al. Low power, low temperature and atmospheric pressure plasma-induced polymerization: facile synthesis and crystal regulation of covalent organic frameworks. *Angew. Chem. Int. Ed.* **60**, 9984–9989 (2021).
40. Wu, C.-J., Shao, M.-Z., Geng, Y. & Dong, Y.-B. Photochemical synthesis of covalent organic frameworks. *ChemCatChem* **15**, e202300244 (2023).
41. Díaz de Greñu, B. et al. Microwave-assisted synthesis of covalent organic frameworks: a review. *ChemSusChem* **14**, 208–233 (2021).

42. Hu, J., Huang, Z. & Liu, Y. Beyond Solvothermal: alternative synthetic methods for covalent organic frameworks. *Angew. Chem. Int. Ed.* **62**, e202306999 (2023).
43. Li, Y., Chen, W., Xing, G., Jiang, D. & Chen, L. New synthetic strategies toward covalent organic frameworks. *Chem. Soc. Rev.* **49**, 2852–2868 (2020).
44. Paul, R. et al. Benzothiazole-linked metal-free covalent organic framework nanostructures for visible-light-driven photocatalytic conversion of phenylboronic acids to phenols. *ACS Appl. Nano Mater.* **4**, 11732–11742 (2021).
45. Wang, P.-L., Ding, S.-Y., Zhang, Z.-C., Wang, Z.-P. & Wang, W. Constructing Robust covalent organic frameworks via multicomponent reactions. *J. Am. Chem. Soc.* **141**, 18004–18008 (2019).
46. Das, P. et al. Integrating bifunctionality and chemical stability in covalent organic frameworks via one-pot multicomponent reactions for solar-driven H_2O_2 production. *J. Am. Chem. Soc.* **145**, 2975–2984 (2023).
47. Li, X.-T. et al. Construction of covalent organic frameworks via three-component one-pot Strecker and Povarov reactions. *J. Am. Chem. Soc.* **142**, 6521–6526 (2020).
48. Wang, G.-B. et al. Construction of covalent organic frameworks via a visible-light-activated photocatalytic multicomponent reaction. *J. Am. Chem. Soc.* **145**, 4951–4956 (2023).
49. Afshari, M., Dinari, M., Farrokhpour, H. & Zamora, F. Imine-linked covalent organic framework with a naphthalene moiety as a sensitive phosphate ion sensing. *ACS Appl. Mater. Interfaces* **14**, 22398–22406 (2022).
50. Nouruzi, N., Dinari, M., Gholipour, B., Afshari, M. & Rostamnia, S. In situ organized pd and au nanoparticles in a naphthalene-based imine-linked covalent triazine framework for catalytic Suzuki reactions and H2 generation from formic acid. *ACS Appl. Nano Mater.* **5**, 6241–6248 (2022).
51. Afshari, M. & Dinari, M. Improving the reaction-to-fire properties of thermoplastic polyurethane by new phosphazene–triazinyl-based covalent organic framework. *ACS Appl. Mater. Interfaces* **14**, 49003–49013 (2022).
52. Asadi, P. et al. Advanced postsynthetic modification of COF: elevating hydrophilicity for efficient doxorubicin delivery. *ACS Appl. Bio Mater.* **8**, 4325–4336 (2025).
53. Grätz, S., Junior, M., de, O., Gutmann, T. & Borchardt, L. A comprehensive approach for the characterization of porous polymers using 13C and 15N dynamic nuclear polarization NMR spectroscopy. *Phys. Chem. Chem. Phys.* **22**, 23307–23314 (2020).
54. Hutsch, S. et al. Mechanochemical cyclotrimerization: a versatile tool to covalent organic frameworks with tunable stacking mode. *Angew. Chem. Int. Ed.* **63**, e202403649 (2024).
55. Harris, K. D. M. & Thomas, J. M. Probing polymorphism and reactivity in the organic solid state using 13C NMR spectroscopy: studies of *p*-formyl-*trans*-cinnamic acid. *J. Solid State Chem.* **94**, 197–205 (1991).
56. Algara-Siller, G. et al. Triazine-based graphitic carbon nitride: a two-dimensional semiconductor. *Angew. Chem. Int. Ed.* **53**, 7450–7455 (2014).
57. Zhao, L. et al. Imidazole-doped cellulose as membrane for fuel cells: structural and dynamic insights from solid-state NMR. *J. Phys. Chem. C*. **120**, 19574–19585 (2016).
58. Volkov, A. et al. General strategy for incorporation of functional group handles into covalent organic frameworks via the Ugi reaction. *J. Am. Chem. Soc.* **145**, 6230–6239 (2023).
59. Knicker, H. & Lüdemann, H.-D. N-15 and C-13 CPMAS and solution NMR studies of N-15 enriched plant material during 600 days of microbial degradation. *Org. Geochem.* **23**, 329–341 (1995).
60. Lyle, S. J. et al. Multistep solid-state organic synthesis of carbamate-linked covalent organic frameworks. *J. Am. Chem. Soc.* **141**, 11253–11258 (2019).
61. Emmerling, S. T., Maschita, J. & Lotsch, B. V. Nitric oxide (NO) as a reagent for topochemical framework transformation and controlled no release in covalent organic frameworks. *J. Am. Chem. Soc.* **145**, 7800–7809 (2023).
62. Tohidi, M. E. & Amiri, A. Literature on the synthesis of modulator-assisted covalent–organic frameworks (MA-COFs): a review. *Adv. Mater* **38**, e11083 (2025).
63. Zhang, Z. et al. Micro/nano-scaled covalent organic frameworks: polymerization, crystallization and self-assembly. *ChemNanoMat*. **8**, e202100345 (2022).
64. Zhang, M. et al. Construction of flexible amine-linked covalent organic frameworks by catalysis and reduction of formic acid via the Eschweiler–Clarke reaction. *Angew. Chem. Int. Ed.* **60**, 12396–12405 (2021).
65. Fan, Y. et al. A case study on the influence of substitutes on interlayer stacking of 2D covalent organic frameworks. *Chem. Eur. J.* **23**, 5668–5672 (2017).
66. Shinde, D. B. et al. Crystalline 2D covalent organic framework membranes for high-flux organic solvent nanofiltration. *J. Am. Chem. Soc.* **140**, 14342–14349 (2018).
67. Liu, Y. et al. Redox-bipolar polyimide two-dimensional covalent organic framework cathodes for durable aluminium batteries. *Angew. Chem. Int. Ed.* **62**, e202306091 (2023).
68. Sing, K. S. Reporting physisorption data for gas/solid systems with special reference to the determination of surface area and porosity (Recommendations 1984). *Pure Appl. Chem.* **57**, 603–619 (1985).
69. Feng, X., Ding, X. & Jiang, D. Covalent organic frameworks. *Chem. Soc. Rev.* **41**, 6010–6022 (2012).
70. Thommes, M. et al. Physisorption of gases, with special reference to the evaluation of surface area and pore size distribution (IUPAC Technical Report). *Pure Appl. Chem.* **87**, 1051–1069 (2015).
71. Puthiaraj, P., Yu, K., Shim, S. E. & Ahn, W.-S. Pd(II)-immobilized on a nanoporous triazine-based covalent imine framework for facile cyanation of haloarenes with K4Fe(CN)6. *Mol. Catal.* **473**, 110395 (2019).
72. Karbalaee Hosseini, A. & Tadjarodi, A. Sonochemical synthesis of nanoparticles of Cd metal organic framework based on thiazole ligand as a new precursor for fabrication of cadmium sulfate nanoparticles. *Mater. Lett.* **322**, 132481 (2022).
73. Prime, R. B., Bair, H. E., Vyazovkin, S., Gallagher, P. K. & Riga, A. in *Thermal Analysis of Polymers: Fundamentals and Applications* (eds Menczel, J. D. & Prime, R. B.) Ch. 3 (John Wiley & Sons, Inc., 2009).
74. Davis, R. E., Bromels, E. & Kibby, C. L. Boron hydrides. III. Hydrolysis of sodium borohydride in aqueous solution. *J. Am. Chem. Soc.* **84**, 885–892 (1962).
75. Wang, C. et al. Insight into the mechanism of gold-catalyzed reduction of nitroarenes based on the substituent effect and in situ IR. *New J. Chem.* **41**, 3865–3871 (2017).
76. Shi, B. et al. Ag nanoparticles encapsulated in carboxyl-functionalized hollow microporous organic nanospheres for highly efficient catalysis applications. *Appl. Catal. A Gen.* **588**, 117276 (2019).

Acknowledgements

We thank Mr. Mohsen Soroushmanesh (IUT) for his assistance with the XRD pattern simulation. We thank Prof. Buntkowsky (TU Darmstadt) for the generous allocation of measurement time at his 400 MHz Bruker DNP NMR spectrometer.

Author contributions

N.S. designed this study, conducted the experiment, analyzed the data, and wrote the paper; J.L., T.G, and K.H.C. assisted with materials characterizations; N.S., T.G., and M.D. discussed the results and commented on the manuscript; and M.D. supervised the project.

Funding
N.S. discloses support for the research of this work from the Iranian National Science Foundation (INSF) [4021419]. T.G. discloses support for the research of this work from the German Science Foundation (DFG) [contract GU-1650/3-2 project number 429632542].

Competing interests
The authors declare no competing interests

Additional information
Supplementary information The online version contains supplementary material available at https://doi.org/10.1038/s42004-026-02095-3.

Correspondence and requests for materials should be addressed to Mohammad Dinari.

Peer review information *Communications Chemistry* thanks the anonymous reviewers for their contribution to the peer review of this work.